Engineering the Mechanics of Heterogeneous Soft Crystals

Hansohl Cho[1], James C. Weaver[2], Elmar Pöselt[3], Pieter J. in't Veld[4], Mary C. Boyce[5†], Gregory C. Rutledge[1,‡]

[1]Department of Chemical Engineering, Massachusetts Institute of Technology, Cambridge, MA 02139

[2]Wyss Institute for Biologically-Inspired Engineering, Harvard University, Cambridge, MA 02139

[3]BASF Polyurethanes GmbH, Elastogranstr. 60, D-49448 Lemförde, Germany

[4]BASF SE, GME/MM, Carl Bosch Str. 38, 67056 Ludwigshafen, Germany

[5]Fu Foundation School of Engineering and Applied Science, Columbia University, New York, NY 10027

Abstract

This work demonstrates how the geometric and topological characteristics of substructures within heterogeneous materials can be employed to tailor the mechanical responses of soft crystals under large strains. The large deformation mechanical behaviors of elastomeric composites possessing long-range crystalline order are examined using both experiments on 3D printed prototype materials and precisely matched numerical simulations. The deformation mechanisms at small and large strains were elucidated for six sets of morphologies: dispersed-particles on each of the simple cubic, body-centered cubic or face-centered cubic lattices, and their bi-continuous counterparts. Comparison of results for the six types of morphologies revealed that the topological connectivity of dissimilar domains is of critical importance for tailoring the macroscopic mechanical properties and the mechanical anisotropy.

1. Introduction

Polymer composites have long been of central importance in a wide range of engineering contexts, by virtue of the synergies in the mechanical[1], chemical[2] and optical[3] properties of their constituent materials. Moreover, polymer composites have advantages over other engineering materials that include scalability, durability, functionality, light weight and relatively low cost.[4] In addition to the intrinsic material properties, the geometric and topological features of their constituents have been shown to influence significantly the structure-property-function relationships in many heterogeneous materials.[5] In particular, a wide variety of microstructural morphologies have been extensively reported in synthetic and natural polymeric systems, including lamellae, spheres or cylinders dispersed within matrices and co-continuous networks.[6] In the copolymeric materials, the morphological features of constituents are strongly dependent on the thermodynamic nature of the constituent polymers via their volume fraction, interaction and miscibility. In particular, the interpenetrating co-continuous networks, in which each component spans the macroscopic materials without any isolated domains, were found to be promising

Correspondence: †boyce@columbia.edu; ‡rutledge@mit.edu

for tailoring the macroscopic physical responses of ordered and disordered copolymeric materials.[7] The co-continuous structures also broaden the range of mechanical and other physical properties over those of the classical dispersed-particle morphologies or lamellar copolymeric morphologies.[8] Moreover, the mechanical features made possible by varying the microstructural morphologies of constituents are critical to achieve tunable acoustical and optical properties especially in photonic and phononic crystals for energy and soft electronics applications.[9] Moreover, composites with various morphologies have been used in the design of soft meta-materials having unconventional functionalities.[10] Such soft materials have been recently used in a wealth of new applications particularly to soft robotics and actuation[11], acoustic manipulation[12], super-hydrophobic surfaces[13] and smart soft structures via instability.[14] In all of these applications, a sound understanding of the large strain deformation mechanisms of soft composites possessing complex geometry and nonlinear constituent behavior is essential. In this work, we address the large strain mechanics of soft crystalline composites whose structural features were inspired by phase-separated block copolymers and crystalline metals. The macroscopic mechanical behavior is elucidated in terms of the morphology, topological connectivity and constitutive properties of the constituent substructures. Soft composites possessing long-range crystalline order were designed and fabricated with a multi-material 3D printer using photo-curable pre-polymers. The nonlinear mechanical responses of these composites under large deformation were then evaluated through both experiments and numerical simulations. The stress-strain behaviors revealed that the topological connectivity within each of the two dissimilar domains plays a critical role in determining the mechanical performance and the anisotropy. Of particular interest is the opportunity to engineer the structure-property relationships of these heterogeneous soft materials by altering the morphology, connectivity and mechanical properties of their constituents.

2. Results and Discussion

2.1. 3D Printed Soft Crystalline Composites

The soft crystalline composites were designed and fabricated to have various mechanical stiffness ratios and volume fractions of their hard and soft components on three Bravais cubic lattices: simple-cubic (SC), body-centered-cubic (BCC) and face-centered-cubic (FCC) systems. In addition to the dispersed-particle composites, their bi-continuous counterparts (denoted SC-Bi, BCC-Bi and FCC-Bi) were also designed. The bi-continuous composites were constructed by simply connecting the first nearest neighbor sites of SC, BCC and FCC lattices with rod-like sections while maintaining the specified volume fractions of hard and soft domains. High-precision geometric information was prepared using a three-dimensional (3D) CAD (computer aided design) program and then sent to a 3D printer (Connex 500, Stratasys Inc.) to build the prototypes. During 3D-printing, multiple photo-curable prepolymers are used to form the hard and soft components. In this work, two miscible base rubbery/glassy materials (TangoPlus^{TM} and VeroWhite^{TM})[15] and their mixtures were used to provide constituents with the desired mechanical properties in the printed prototypes. Pure TangoPlus, which is highly rubbery, was used for the soft domains (labeled "s") in all prototypes. Mixtures of TangoPlus and VeroWhite with a wide range of initial stiffnesses relative to the soft component, formed via a digital material mode in the printer, were used for the hard component (labeled "h1", "h2", "h3" and "h4"). The initial stiffness ratios of the hard to the soft component were ~3.5, ~5.2, ~9.5 and ~15 for the composition pairs h1/s, h2/s, h3/s and h4/s, respectively; in addition, the composition pair h5/s having a stiffness ratio of ~100 was used for simulation only. Detailed characterization of the stress-strain behaviors of the hard and soft materials is provided in the **Appendix** along with the material constitutive models used in the numerical simulations. The volume fractions of hard components were 50% or 25% for each of the six morphologies examined in experiments: SC, SC-Bi, BCC, BCC-Bi, FCC and FCC-Bi. For each morphology, both "*hard-in-soft*" (soft component used as matrix) and "*soft-in-hard*" (hard component used as matrix) composites were fabricated and tested in both experiments and simulations. Each printed prototype comprised 5 unit cells in each dimension. The unit cell dimension was 5 mm, resulting in prototype dimensions of 25 mm by 25 mm by 25 mm. The minimum geometric size of inner structures in the crystalline composites was ~ 0.78 mm, which is at least one order of magnitude greater than the minimum resolution (< ~0.025 mm) provided by the 3D printer. **Figure 1** shows schematics of the soft crystalline composites in BCC (**Figure 1a**), SC (**Figure 1b)** and FCC (**Figure 1c**) lattices, along with optical images of the printed prototypes. In the images of printed prototypes, the bright regions represent the hard domains while the dark regions represent the soft domains. The bi-continuous variants denoted SC-Bi, BCC-Bi and FCC-Bi were also fabricated with the same base materials and volume fractions for hard and soft domains as the dispersed-particle SC, BCC and FCC composites.

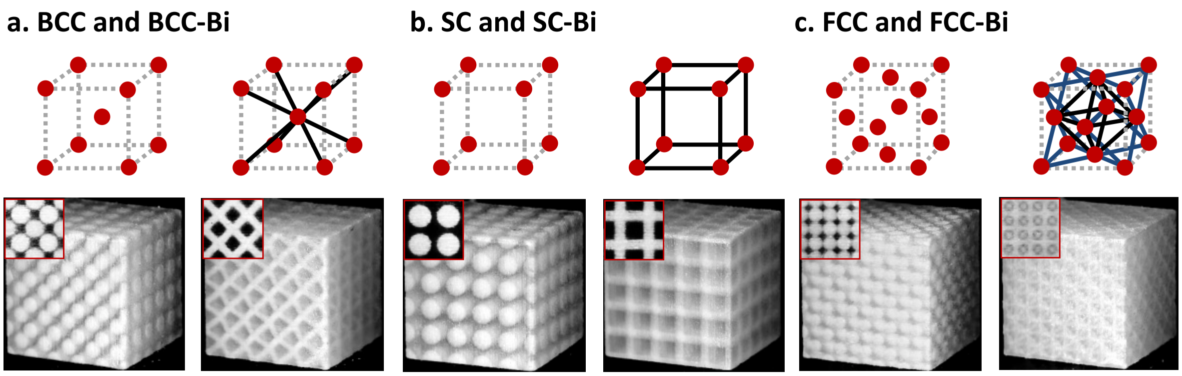

Figure 1 Schematic representations of soft crystalline composites. (a) BCC, (b) SC, (c) FCC; First row: unit cells for dispersed-particle and bi-continuous composites (solid lines: 1st nearest neighbor pairs for rod-connection); Second row: optical images (insets: front views of central 2 by 2 unit cells) of the 3D-printed composite prototypes; here, the volume fraction of hard (bright domains)/soft domains (dark domains) is 25%/75% and the number of unit cells is 5 by 5 by 5).

2.2. Large Deformation Behavior of Soft Crystalline Composites

Mechanical behavior of the soft crystalline composites was examined under finite uniaxial compression in both experiments and numerical simulations. The 3D printed prototypes were compressed between two well-lubricated steel plates using a mechanical testing machine (Z010, loadcell: 2.5 kN, Zwick-Loewel). Under compression, force-displacement data were recorded and deformation of the prototypes was carefully monitored photographically to confirm macroscopic homogeneity of deformation throughout the periodic unit cells in the finite-sized prototypes. Numerical simulations were also performed on each of morphologies, using finite element computations. A Neo-Hookean hyperelastic representation was used for constitutive behaviors of the constituent materials. The macroscopic composite behaviors were analyzed using representative volume elements (RVE) subjected to a generalized three-dimensional periodic boundary condition, which is appropriate for finite deformation analysis. Moreover, the interfaces between the hard and soft domains were assumed to be perfectly bonded under deformation in either experiments or numerical simulations. Detailed information on the finite strain RVE analysis, boundary conditions and constitutive models is provided in the **Appendix**.

The stress-strain behaviors of the BCC composites are presented in **Figure 2a**, and the stress amplification (i.e. the composite stress normalized by the soft component response) are presented in **Figure 2b** along with representative optical images of the composite prototypes under deformation (dispersed-particle in **Figure 2c** and bi-continuous in **Figure 2d)**. The stress amplification measure (normalized stress) is used throughout this work since it shows more clearly the relative changes in the macroscopic composite behaviors, especially for finite deformation, in both experiments and numerical simulations. Here, the volume fraction of hard components was 50% and the stiffness ratios were ~3.5 (h1/s), ~5.2 (h2/s), ~9.5 (h3/s), ~15 (h4/s) and ~100 (h5/s) for the *"hard-in-soft"* composites. The numerically predicted stress-strain curves match well the experimental data, for a range of different constitutive properties of hard components with the same soft component. The macroscopic stresses were greater in the bi-continuous composites at small to large strains, compared to those in the corresponding dispersed-particle composites, in both experiments and simulations; furthermore, the difference between macroscopic stresses in the bi-continuous and dispersed-particle morphologies increased with an increasing stiffness ratio. In particular, there was a substantially enhanced stiffening effect (factors of ~4.5 and ~1.3 at macroscopic strains of 0.05 and 0.4) due to the change in connectivity from BCC to BCC-Bi at the highest stiffness ratio of ~100 (h5/s, inset of **Figure 2a**). **Figure 2c** and **Figure 2d** show selected optical images of two illustrative cases, the BCC and BCC-Bi composites with h3/s ~ 9.5 under deformation. As shown in the optical images, macroscopically homogeneous deformation was observed during experiments on these finite-sized periodic prototypes.

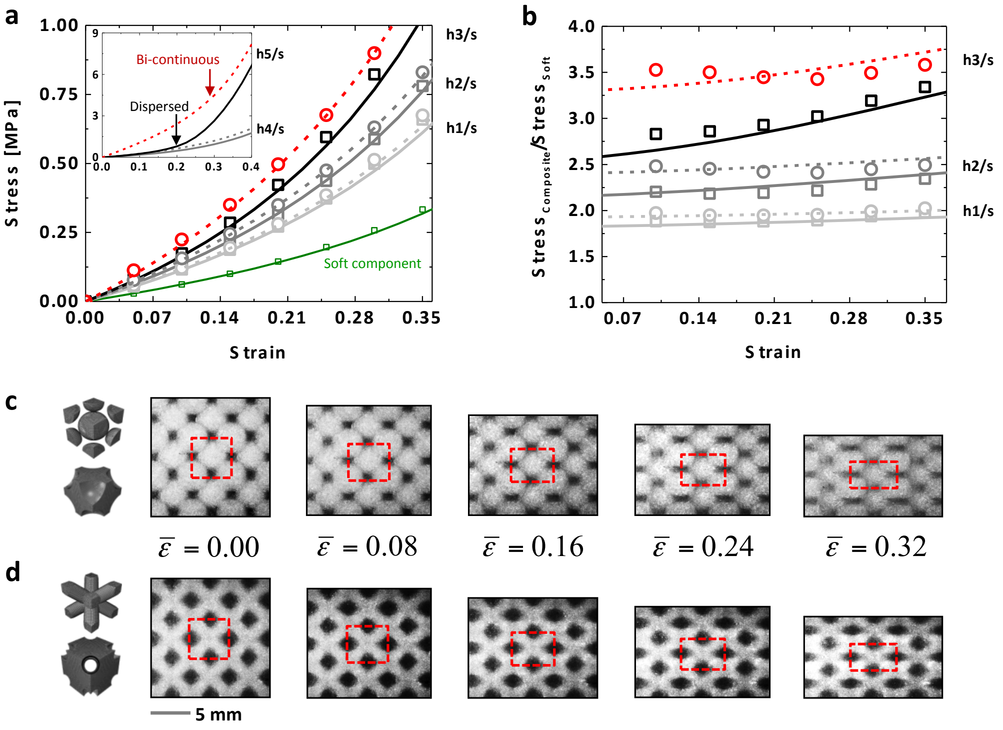

Figure 2 Large deformation mechanical behavior of soft crystalline composites in the BCC lattice with equal volume fractions of hard/soft domains. (a) Representative stress-strain curves of BCC (squares, solid lines) and BCC-Bi (circles, dashed lines) composites (symbols: experiment, lines: simulation) at increased stiffness ratios (h1/s~3.5, h2/s~5.2 and h3/2 ~ 9.5) together with the soft component response (green symbols and lines); inset: simulated stress-strain curves at higher stiffness ratios of ~15 (h4/s) and ~100 (h5/s); (b) Stress amplification (composite stress normalized by soft component response) in experiments and simulations in the dispersed-particle and bi-continuous morphologies with increased

stiffness ratios; Representative experimental images of (c) BCC (v_{hard}=50%) and (d) BCC-Bi (v_{hard}=50%) morphologies under compression; here, only the central 3 by 3 unit-cells are shown; the dashed rectangle highlights the central unit cell in the composites; the far left figures illustrate the hard inclusions (green) and the soft matrices (grey) in the unit cell.

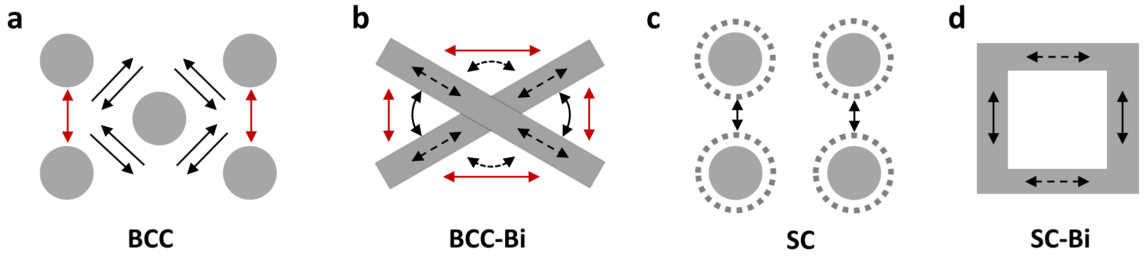

Figure 3 Schematics of deformation mechanisms in BCC and SC lattice. (a) BCC; (b) BCC-Bi; (c) SC (the dashed particles at a higher hard volume fraction which is comparable to the corresponding SC-Bi composite); (d) SC-Bi; here only the hard domains are illustrated on the 110 and 100 planes, for BCC and SC lattices, respectively; the solid/dashed black arrows represent major deformation modes at small strain while the red arrows represent those at large strain

The deformation mechanisms of these composites are schematically illustrated in **Figure 3a**. At small strains in the dispersed-particle BCC composite, an off-axis shearing between the nearest neighbor particles (on 110 planes) carries the applied deformation predominantly. As the off-axis shearing decreases, a co-axial and center-to-center interaction between the second nearest neighbor hard particles becomes more significant, resulting in a stress upturn at large strains. However, in the bi-continuous BCC composite, deformation is carried by bending and stretching of the relatively stiff ligament network with the rotation necessitating compression and tension in the soft matrix as illustrated in **Figure 3b**. This interpretation of the deformation mechanisms in these two morphologies is also supported by the local stress and strain contours from the numerical simulations. **Figure 4** shows the contours of local equivalent stress (von Mises stress) and axial strain in the dispersed-particle and bi-continuous BCC composites with two different stiffness ratios of ~9.5 (h3/s) and ~100 (h5/s). As presented in **Figure 4a,** large strains were initially localized within the soft matrix since deformation was predominantly carried by the soft matrix in the dispersed-particle composite. Additionally the off-axis interactions between the first nearest neighbor particles initially resulted in a relatively small deformation of the hard particles. Direct and co-axial interactions between the second nearest neighbor particles then resulted in very large stresses localized within the hard particles at large strains (**Figure 4c**). However the presence of a ligament network in the bi-continuous composite resulted in development of the substantially large stresses and strains localized in the hard domains as shown in **Figure 4b** and **Figure 4d**. The localized large deformation in the ligament network led to the greater macroscopic stress responses at both small and large strains. The contours of local stress and strain fields are further presented for the composites with a lower stiffness ratio in **Figure 4e** and **Figure 4f**. The local deformations in the hard domains with the lower stiffness ratio (h3/s ~ 9.5) were found to be much greater than those with the higher stiffness ratio (h5/s ~ 100, **Figure 4c** and **Figure 4d**) for both morphologies. The larger deformations in the hard domains, more comparable to the extreme deformations in the soft domains, substantially diminished the morphological effects in the composites with the lower stiffness ratios, as evidenced by the macroscopic stress-strain curves in **Figure 2**.

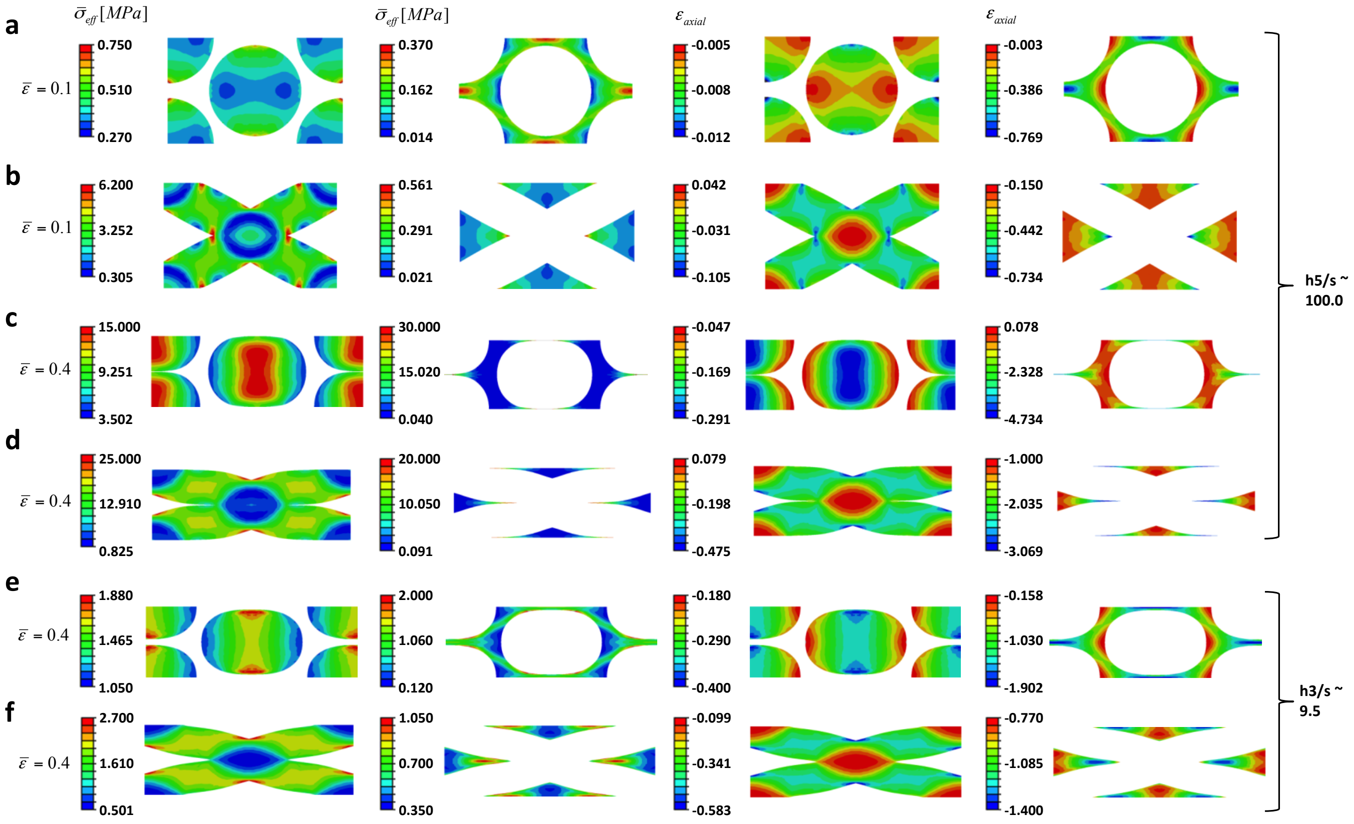

Figure 4 Contours of local stress and strain fields in BCC and BCC-Bi composites with stiffness ratios of 9.5 (h3/s) and 100 (h5/s). Equivalent stress (von Mises stress) and axial true strain (the Hencky's logarithmic strain) in both hard and soft domains with h5/s ~ 100 (a) BCC at a strain of 0.1; (b) BCC-Bi at a strain of 0.1; (c) BCC at a strain of 0.4; (d) BCC-Bi at a strain of 0.4 and in the composites with h3/s ~ 9.5 (e) BCC at a strain of 0.4; (f) BCC-Bi at a strain of 0.4; here the cutting plane for the contours is 110 on the center of unit cell and the volume fraction of hard component is 50%.

The morphological effects are next examined in composites on the FCC lattice, for both experiments and simulations. **Figure 5** shows the stress-strain behavior of the FCC composites in experiments and simulations. Here, the volume fractions of hard and soft components were 50%/50% and 25%/75%, and the stiffness ratio was ~9.5 (h3/s). The numerically predicted stress-strain curves show a good agreement with the experimental data using the same constitutive laws as those used in the BCC composites. The stress responses of the bi-continuous composites were greater, by a factor of ~1.35, relative to those of the dispersed-particle composites. The deformation mechanisms in these FCC composites were very similar to those in the BCC composites especially for the dispersed-particle morphology. However, the stiffening effect due to the change in connectivity was greater than that found in the BCC lattice (a factor of ~1.17 with h3/s ~ 9.5), as evidenced from comparison of the normalized stress-strain curves in **Figure 2b** (BCC) and **Figure 5b** (FCC). The greater stiffening effect is mainly attributed to a higher packing density in the FCC lattice. In the dispersed-particle FCC composite, off-axis shearing interactions between the close-packed particles on the 100 planes were responsible for a lower stress response and remained significant over all strains. Meanwhile, deformation in the bi-continuous FCC composite was consistently dominated by bending and rotation throughout the denser ligament network, as was the case for the bi-continuous BCC composite, and there was no significant change in the major local deformation modes at increasing strains. The stiffening effect due to the change in connectivity from dispersed-particle to bi-continuous is relatively insensitive to the imposed strains in the FCC lattice as shown in **Figure 5b**, in contrast to the BCC.

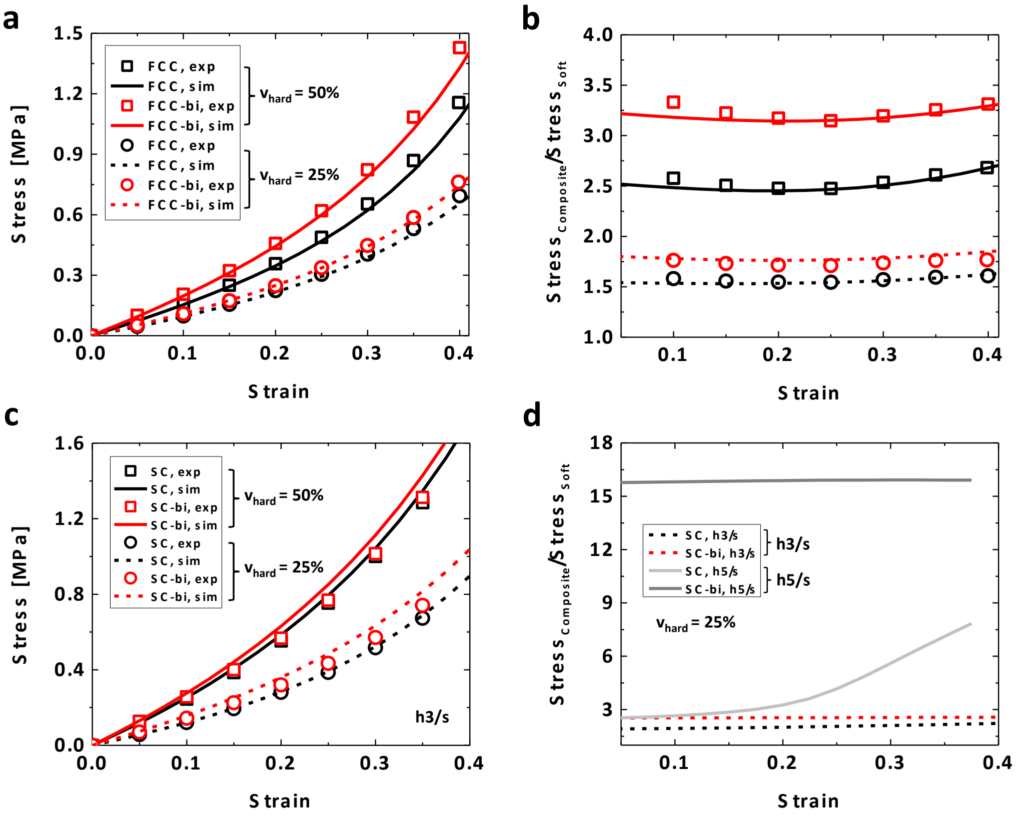

Figure 5 Large deformation mechanical behavior of soft crystalline composites in the FCC and SC lattices at two different volume fractions of hard component (25% and 50%). (a) Representative stress-strain curves (symbols: experiment, lines: simulation); (b) Stress amplification (composite stress normalized by soft component response) in FCC and FCC-Bi; here the stiffness ratio of hard/soft component is ~9.5 (h3/s); (c) Stress-strain curves; (d) Stress amplification (v_{hard} = 25%) in SC and SC-Bi at increasing stiffness ratios of ~9.5 (h3/s) and ~100 (h5/s).

The large deformation mechanical behaviors for the dispersed and bi-continuous composites were then examined for the SC lattices, as shown in **Figure 5c** and **d**. The stress-strain behaviors in these two composites were much stiffer than those in either BCC or FCC composites. Nevertheless, the bi-continuous morphology still exhibited a greater stress response than the dispersed-particle morphology over all strains. Interestingly, this stiffening effect was lessened at the higher volume fraction of hard component (50%), which is contrary to that found in the FCC composites (**Figure 5b**). The hard particles are very close to each other at this high volume fraction. Therefore, direct, coaxial interactions between the particles led to a very hard lattice resistance in the dispersed-particle morphology as schematically illustrated in **Figure 3c**, such that the stress response was comparable to that of the bi-continuous morphology. At the lower volume fraction of hard component (25%), the stiffening effect was greater, which resulted from substantial stretching throughout the orthogonal truss-like ligament network as illustrated in **Figure 3d**. The stiffening effect was again found to increase with a higher stiffness ratio of hard to soft component as shown in the normalized stress responses in **Figure 5d**.

The mechanical behaviors of the composites are summarized for the six morphologies with the two stiffness ratios of hard/soft component (h3/s ~ 9.5 and h5/s ~ 100). **Figure 6a** shows the initial elastic moduli (i.e. at small strains) of the composites in experiments and simulations. In all lattices, the initial elastic modulus was greater in the bi-continuous morphologies than in the dispersed-particle morphologies due to the stretching localized within the relatively stiff ligament network. The initial stiffening effects due to change in morphology from dispersed-particle to bi-continuous in the FCC and BCC composites were much greater than those in the SC composites in both experiments and simulations at this high volume fraction of hard component (50%). The stiffening effect increased substantially in all lattices with increasing stiffness ratio of hard/soft component as shown in **Figure 6b**. At the highest stiffness ratio (h5/s ~ 100), the maximum achievable elastic modulus (in the bi-continuous SC composite) was greater by a factor of ~ 10 than the smallest elastic modulus (in the dispersed-particle BCC or FCC composites). The large strain behaviors of the composites are then presented especially for the bi-continuous morphology in **Figure 6c**. The macroscopic stress was found to increase from FCC-Bi and BCC-Bi to SC-Bi composites, as evidenced by both experiments and simulations. As the stiffness ratio of hard to soft domains increases (inset of **Figure 6c**), the stress-strain behavior was most affected in the SC composite. **Figure 7a** shows the local stress and strain contours at a macroscopic strain of 0.4; a very large compressive strain was localized within the vertical ligaments, resulting in a highly stiffened response in the SC-Bi composite. By contrast, in the BCC-Bi (**Figure 7b**) and FCC-Bi (**Figure 7c**) composites, the applied deformation was more evenly distributed throughout the ligament network, resulting in much smaller axial stresses and strains in these composites, compared to those of the SC-Bi composite. In particular, the ligament network throughout the close-packed FCC lattice carried the macroscopic axial deformation most uniformly by substantial rotation and bending, observed at both small and large strains. Such bending and rotation-dominated deformation modes enabled the most efficient and consistent load transfer mechanism without any significant change in the major deformation modes increasing strain in the FCC-Bi composite. However, there was a major mode change from the bending- and rotation-dominated to the stretching-dominated deformation in the BCC-Bi composite, resulting in a stress upturn at large strain. Such a mode change was found to be significant especially at the highest stiffness ratio (h5/s ~ 100). Though the initial elastic modulus was slightly smaller in the BCC-Bi composite (**Figure 6b**), the macroscopic stress in the BCC-Bi composite became much greater than that of the FCC-Bi composite due to the deformation mode change around a macroscopic strain of 0.2 (the inset of **Figure 6**).

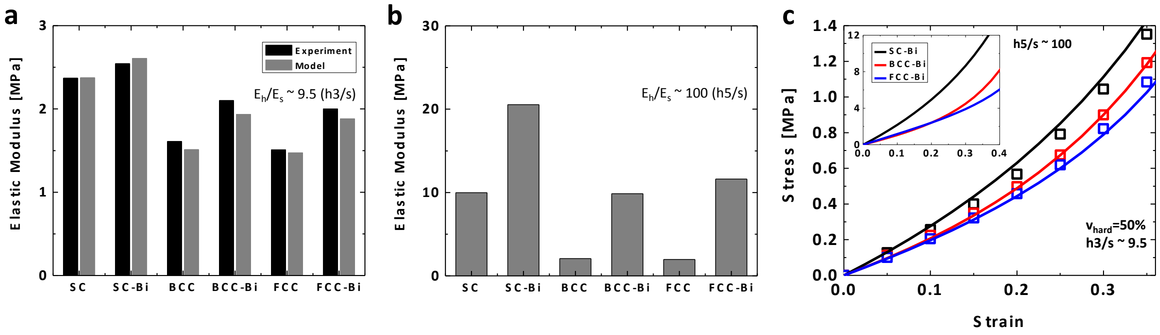

Figure 6 Mechanical behaviors of the composites (v_{hard} = 50%) at small to large strains at two stiffness ratios of hard/soft component (h3/s and h5/s). Young's modulus with (a) h3/s ~ 9.5 (experiment and simulation); (b) h5/s ~ 100 (simulation only); (c) Representative stress-strain behaviors of the bi-continuous composites (experiment: open symbols; simulation: solid lines); here the volume fraction of hard component is 50% and the stiffness ratio is h3/s ~ 9.5 (inset: simulated stress-strain curves with h5/s ~ 100)

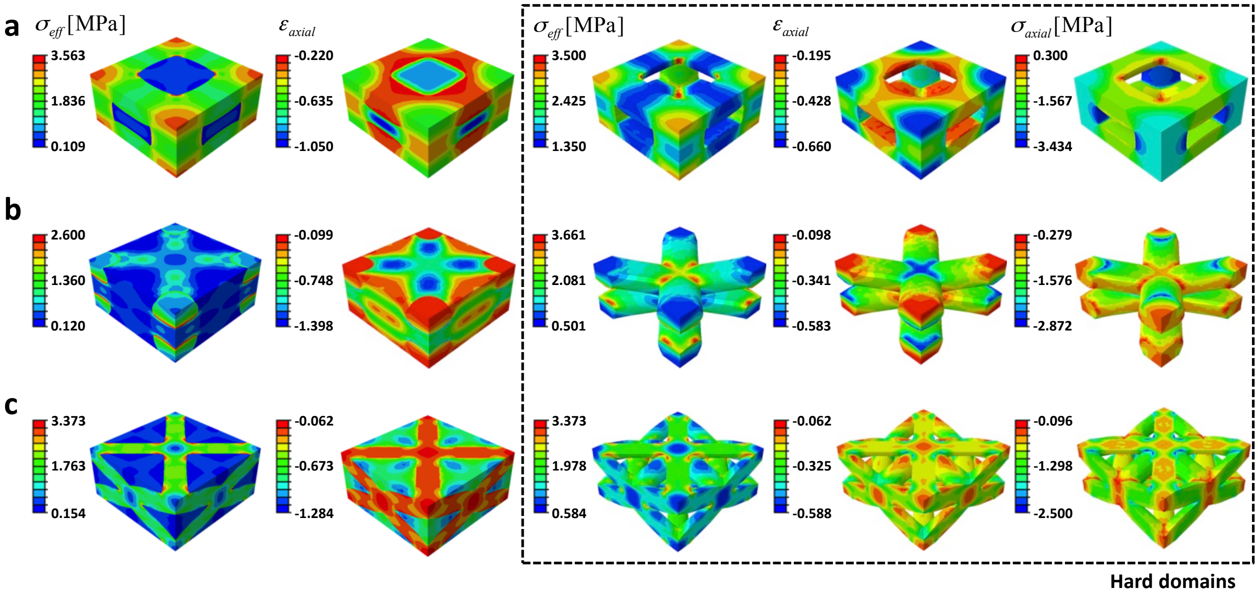

Figure 7 Contours of local stress and strain fields (von Mises equivalent stress, axial true strain and axial true stress). (a) SC-Bi; (b) BCC-Bi; and (c) FCC-Bi at a macroscopic strain of 0.4; here the volume fraction of hard component is 50%, the stiffness ratio of hard/soft component is ~9.5 (h3/s) and the contours of hard domains are shown in the dashed box.

Next, the volume fraction-dependence of stiffness is illustrated for all lattices using a specified stiffness ratio of hard/soft component (h4/s ~ 15). **Figure 8** shows the simulated stress-strain curves of the composites on all of the SC (**Figure 8a**), BCC (**Figure 8b**) and FCC (**Figure 8c**) lattices. Here, the composite stresses were normalized by the soft component response for both the dispersed-particle and bi-continuous morphologies. Comparison of the normalized stresses shows the stiffer mechanical behavior of the bi-continuous morphologies for all lattices and volume fractions. In the dispersed-particle composites, a substantial stress upturn was found due to the onset of significant interactions between the hard particles at large strains. In such cases, the stiffening effect due to the connectivity change was less pronounced at large strains. Interestingly, the major deformation mode was found to vary in the bi-continuous composites over a range of imposed strains. The major mode was predominantly stretching in the SC-Bi composite, resulting in much greater stress responses. In contrast, the major deformation modes were predominantly bending and rotation in the FCC-Bi composite, leading to substantially lower stress responses. The normalized stresses in these SC-Bi and FCC-Bi composites were relatively uniform at all strains. However, there was a clear transition from the bending- and rotation-dominated to the stretching-dominated mode in the BCC-Bi composites, which resulted in a remarkable stress upturn at large strains. The simulated results were further shown for the stiffness increase as a function of hard component volume fraction (the far right column in **Figure 8**). The stiffening effect decreased as the volume fraction of hard component increased in the SC lattice, which was experimentally evidenced in **Figure 5**. In contrast, the stiffening effect increased monotonically in the BCC lattice, and saturated around 50 ~ 60% hard component. The increased stiffening effect was also observed on the FCC lattice up to the equal fractions of hard and soft components. However, at the highest volume fractions (60 ~ 70% hard component), the stiffening effect began to diminish. Very strong co-axial interactions between the second nearest neighbor particles (on each corner of the unit cell) are responsible for the lessened stiffening at these higher volume fractions of hard component.

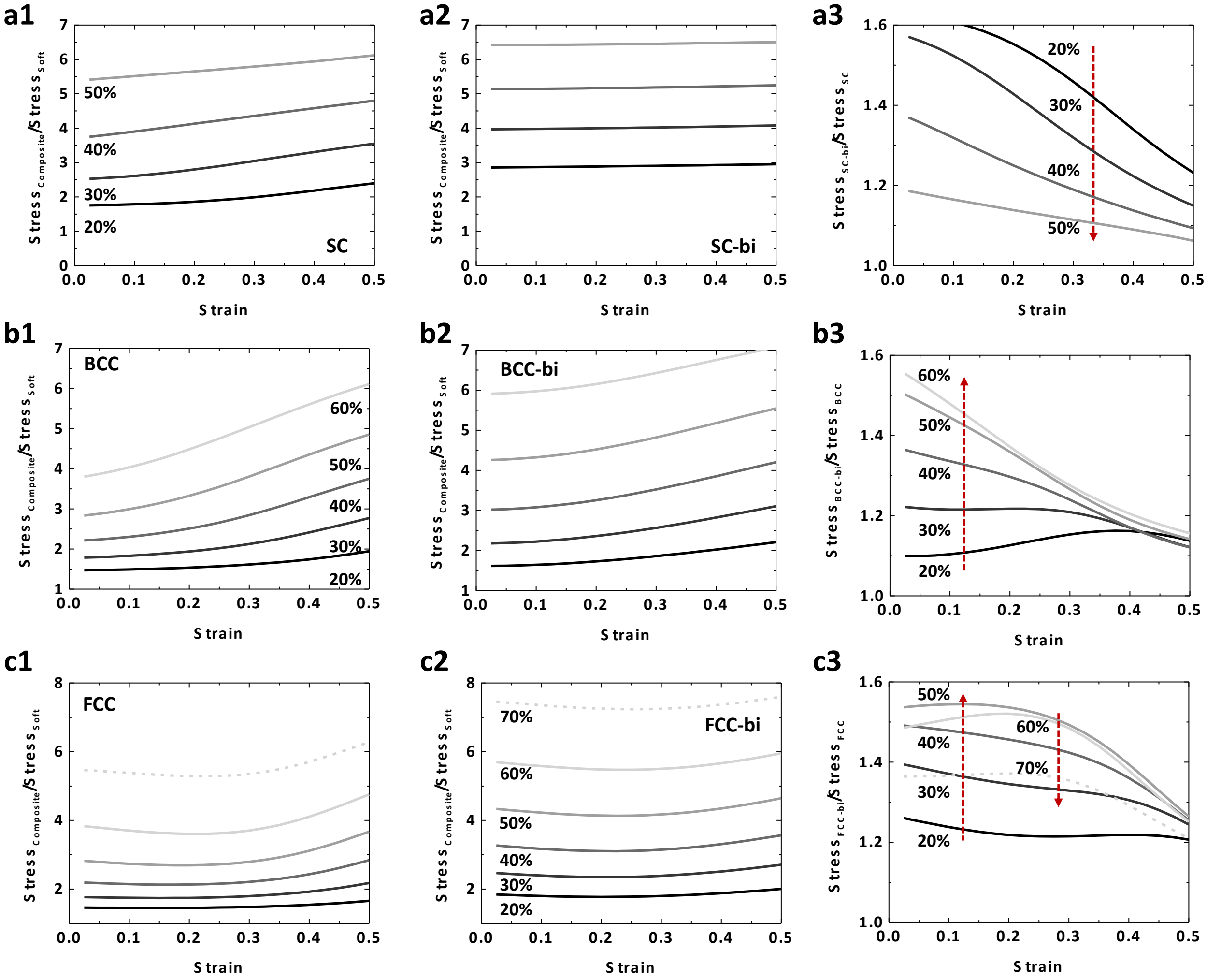

Figure 8 Stiffening effect as a function of volume fractions of hard/soft component obtained by numerical simulations: (a) SC and SC-Bi; (b) BCC and BCC-Bi; (c) FCC and FCC-Bi; (1 and 2: composite stresses normalized by the soft component stress, 3: stiffening factor, here the stiffness ratio of hard to soft component is h4/s ~ 15)

2.3. Mechanical Anisotropy

Long-range order in synthetic and natural materials often leads to anisotropy of the mechanical behavior. In particular, single crystals with SC, BCC and FCC lattices exhibit substantial anisotropic elasticity due to their symmetry features. Here, anisotropy maps are presented especially for small strains using micromechanical models of representative volume elements (RVE) of the six different morphologies (SC, SC-Bi, BCC, BCC-Bi, FCC and FCC-Bi) with a broad range of volume fractions of constituents. In a single crystal having the cubic symmetry, the anisotropy ratio is a non-dimensional parameter, $a \equiv 2C_{44}/(C_{11} - C_{12})$, that is strongly dependent on the magnitude of stiffness in the [111] direction relative to that in the [100] direction.[16] The anisotropy ratio hence provides a quantitative measure of how the directional mechanical stiffness varies with the crystallographic orientation. We computed the three independent elastic moduli of unit cells for all composites that are cubic-symmetric, using several different deformation conditions in simulations. Moreover, we examined the anisotropy change due to a change in a composite "type" from *hard-in-soft* to *soft-in-hard* at equal volume fractions especially for the bi-continuous morphology. **Figure 9a** illustrates the representative volume elements (only hard domains shown here) for the three different bi-continuous morphologies (SC-Bi, BCC-Bi and FCC-Bi highlighted in the blue, red and yellow boxes, respectively) with the two different composite types (*hard-in-soft* and *soft-in-hard*). When constructing the *soft-in-hard* composites with the bi-continuous morphologies, the hard domain in the *soft-in-hard* composites was replaced by a network of rods and connections that reproduces the topological connectivity of the surrounding matrix; it should be noted that the *soft-in-hard* composites were not constructed by simply reversing the composition for the inner ligaments and the surrounding matrices. Therefore, the connectivity of ligaments in the bi-continuous, *soft-in-hard* composites is topologically equivalent to that of the surrounding matrices in the dispersed-particle composites.

The anisotropy maps for these composites are presented for two different volume fractions of hard component (20% and 50%) in **Figure 9b** and **Figure 9c**. Here the magnitude of the vector on each crystallographic orientation represents the "relative" stiffness, or stiffness normalized by that in the [100] direction. If the material is isotropic ($a = 1$), the three dimensional shape is a unit sphere, resulting in further reduction in the number of independent elastic moduli (namely $C_{44} = (C_{11} - C_{12})/2$). The three-dimensional maps of relative stiffness were constructed using Equation (7) and (8) provided in the **Appendix**. At the lower volume fraction of hard component (20%), the bi-continuous morphology exhibited greater anisotropy than the dispersed-particle morphology in all of SC, BCC and FCC lattices as shown in **Figure 9b**. Rod-connecting throughout the nearest neighbors resulted in a substantially increased stiffness in the [111] direction in the BCC and FCC lattice, while it led to a remarkably decreased [111] stiffness in the SC lattice at this particular volume fraction. However, rod-connecting for the bi-continuous morphologies diminished the anisotropy for all lattices in the *hard-in-soft* composites at the equal fractions of hard and soft components (**Figure 9c**). The anisotropy in these composites is, therefore, strongly dependent on the volume fraction of hard/soft component as well as the change in connectivity. Moreover, the change of composite type from *hard-in-soft* to *soft-in-hard* composites also suppressed the anisotropy at the equal volume fractions, except for the BCC-Bi. Interestingly, the change from *hard-in-soft* to *soft-in-hard* influenced the anisotropy significantly in the BCC-Bi. In the *hard-in-*

soft composition, deformation was dominated by bending and rotation modes in the [100] direction, which led to much more compliant behavior in that direction. However, in the *soft-in-hard* composite, deformation was dominated by bending and rotation modes in the [111] direction (or by stretching mode in the [100] direction). Moreover, in the FCC-Bi, deformation of the *soft-in-hard* composite was still dominated by the bending and rotation modes in the [100] direction throughout the relatively stiff ligament networks.

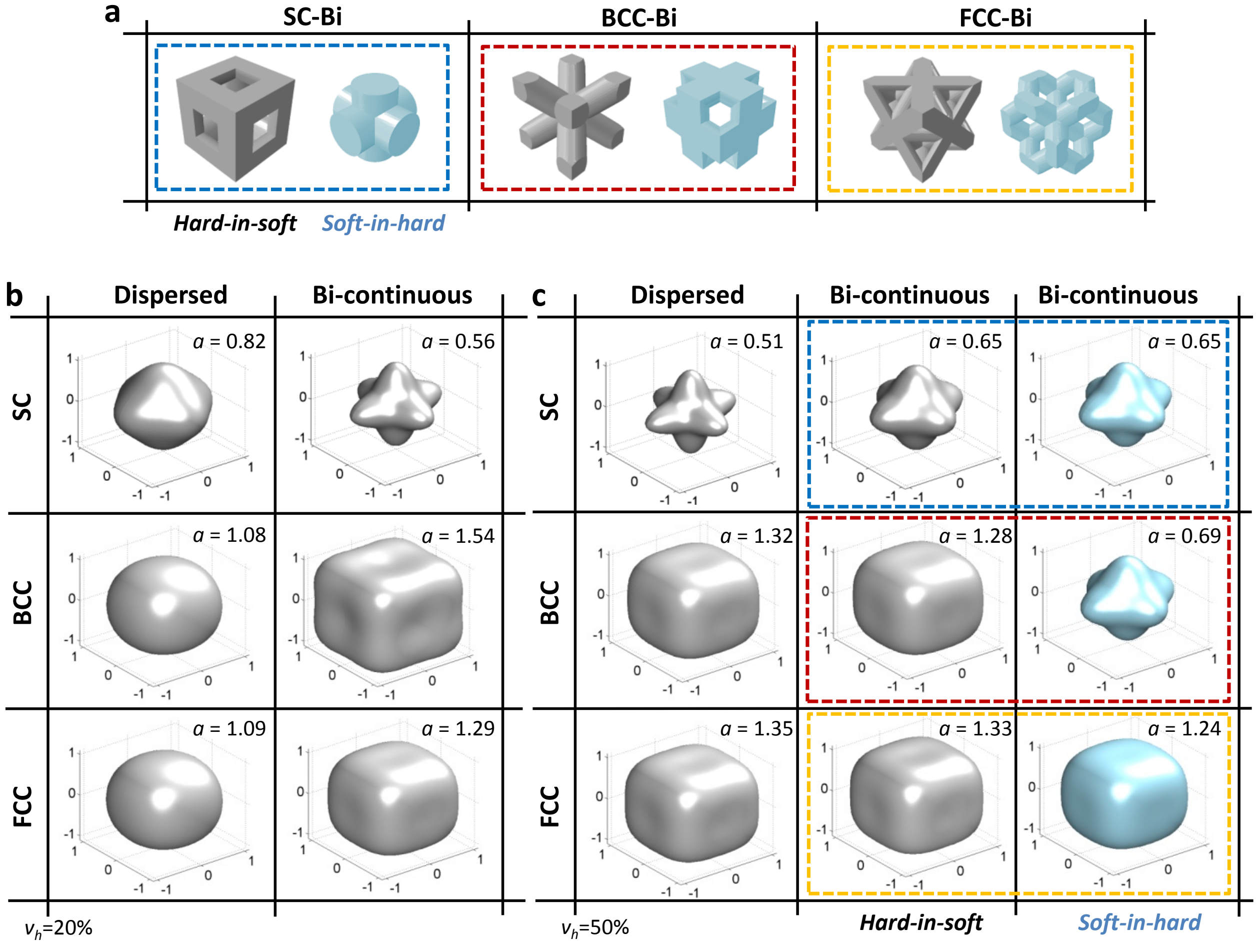

Figure 9 Three-dimensional maps of stiffness as a function of loading direction in the SC, BCC and FCC lattice. (a) Unit cells depicting hard domains in bi-continuous SC, BCC and FCC morphologies in two different composite types: *"hard-in-soft"* and *"soft-in-hard"*; Anisotropy maps of (a) composites with volume fraction: 25%/75% for *hard-in-soft* composites; (b) composites with volume fraction: 50%/50% for *hard-in-soft* and *soft-in-hard* composites; here the stiffness ratio is h4/s ~ 15; *a* is the anisotropy ratio; and the magnitude of each vector on the surface represents the directional stiffness relative to that in the [100] direction

The effect of change in the composite type from *hard-in-soft* to *soft-in-hard* in the bi-continuous morphology is addressed for the mechanical behaviors of the BCC and FCC composites in **Figure 10**. The corresponding RVEs for the hard domains are presented in **Figure 9a** (BCC highlighted by the red dashed box and FCC highlighted by the yellow dashed box). In the BCC lattices (**Figure 10a**), the *soft-in-hard* composites exhibited much stiffer behavior, compared to the *hard-in-soft* composites. This behavior resulted from a change in the major deformation mode to stretching in the [100] direction. The change in deformation mode became more significant with increasing stiffness ratio. In the bi-continuous FCC morphology, the stress-strain behavior was again stiffened, in particular, at large strains in the two material pairs of h3/s ~ 9.5 and h4/s ~ 15, as shown in **Figure 10b**. The overall stiffening effect due to the change in composite type was much smaller for the FCC-Bi composites than that observed in the BCC-Bi composites. The ligament network was geometrically similar to the surrounding matrix in the close-packed FCC lattice, so that deformation was still dominated by bending and rotation modes in the [100] direction, which is comparable to that in the *hard-in-soft* composites.

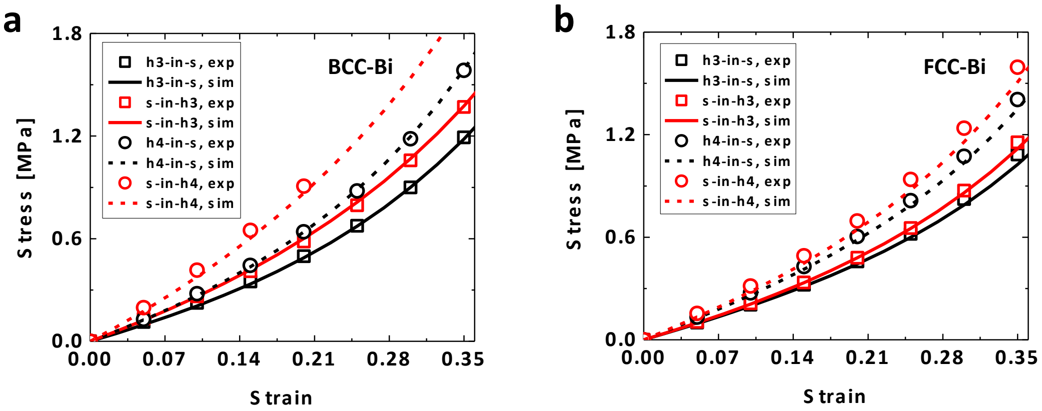

Figure 10 Effect of change of composite type (*hard-in-soft* and *soft-in-hard*) in bi-continuous BCC and FCC composites at two different stiffness ratios of hard to soft components (h3/s ~ 9.5 and h4/s ~ 15). (a) Stress-strain curves in BCC-Bi (b) Stress-strain curves in FCC-Bi

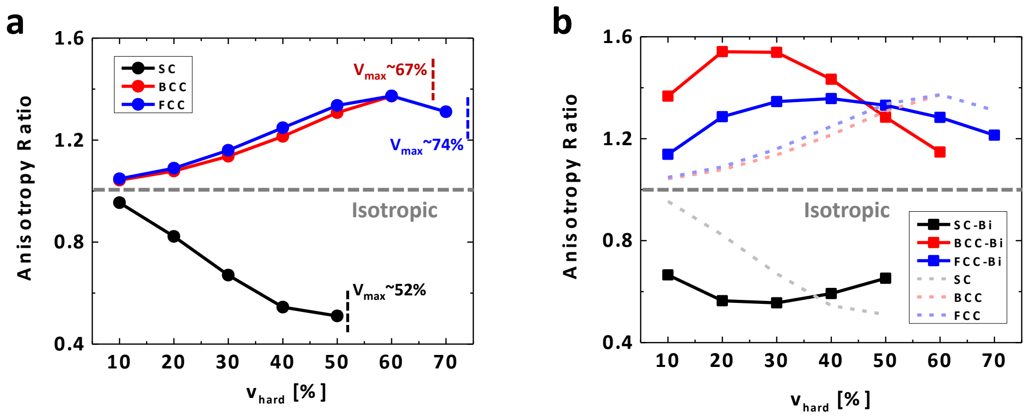

Figure 11 Anisotropy as a function of hard component volume fraction. (a) Anisotropy ratio in the dispersed-particle composites; (b) Anisotropy ratio in the bi-continuous composites (with h4/s ~ 15)

Figure 11 shows the anisotropy of dispersed-particle and bi-continuous composites as a function of an increasing volume fraction of hard component up to the maximum hard component volume fractions achievable in each lattice (SC: ~ 52%, BCC: ~ 67%, and FCC: ~ 74%). Over a broad range of volume fractions, the rod-like ligaments in the bi-continuous morphologies influenced substantially the anisotropy in these crystalline composites, especially in the SC and BCC lattices. However, the anisotropy was less influenced by topological connectivity in the FCC lattice; this was attributed to the fact this lattice has the densest network of hard ligaments. In the dispersed-particle morphologies, anisotropy increased monotonically as the volume fraction of hard components increased, especially in the SC and BCC lattices. Interestingly, while the maximum anisotropy was located near the maximum achievable hard component volume fractions in the dispersed-particle composites, it was observed at the particular fractions of ~20%, ~30% and ~40% for the bi-continuous BCC, SC and FCC composites, respectively. The anisotropy ratio was close to ~1, indicative of nearly isotropic behavior, in the very dilute dispersed-particle composites ($v_{hard} = 10\%$), while significant anisotropy was observed at this low volume fraction of hard component in the bi-continuous composites. The hard network in these dilute bi-continuous composites was responsible for significant increases in the anisotropy in each of the crystal lattices. Furthermore, the dispersed-particle morphologies became more anisotropic than the bi-continuous morphologies for SC, BCC and FCC at volume fractions of ~35%, ~50% and ~50%, respectively. That is, the bi-continuous morphologies were more isotropic at the higher volume fractions of hard components than the dispersed-particle morphologies.

3. Conclusion

In this work, we examined the large strain mechanics of heterogeneous soft crystals through direct mechanical testing on 3D-printed prototypes and through numerical simulations. Multi-material 3D printing was used to design and fabricate precisely a set of representative composite prototypes with not only a wide range of constituent properties and volume fractions, but also a variety of morphologies. The heterogeneous soft crystals were prepared on SC, BCC or FCC lattices with either dispersed-particle or bi-continuous morphologies and with either *hard-in-soft* or *soft-in-hard* composite types. The results from these studies demonstrated that the topological connectivity of these heterogeneous soft crystals were critically influential in tailoring their large deformation mechanical features in tandem with the intrinsic material properties of the constituents and their volume fractions. The experimentally observed large strain mechanical responses were described quantitatively using numerical models with nonlinear elastic constitutive properties for the individual components; analysis of local stress and strain distributions within the numerical models then allowed a detailed examination of the dominant deformation mechanisms in each case. The bi-continuous composites, where the two domains are interpenetrating without any isolated regions, exhibited mechanical performance superior to the classical dispersed-particle composites for the same lattice symmetries, by a combination of various deformation modes operative throughout the interpenetrating ligament networks. The mechanical anisotropy and its variations were also quantified using the micromechanical models over the same wide range of morphologies and volume fractions of components. The mechanical stiffnesses of these composites were strongly dependent on crystallographic orientation, thereby revealing another means for tailoring the mechanical responses. By extension, this work offers a first step towards designing the structure-property relationships of morphologically more complex phase-separated block copolymeric materials, such as thermoplastic copolymers, in which the large strain features are significantly influenced by the topological connectivity, volume fractions and nonlinear constitutive properties of the hard and soft components. Moreover, the new representative volume elements especially for the bi-continuous morphologies can be directly employed for tailoring large strain mechanical responses of cellular materials.

Appendix

- **Micromechanical models under 3D periodic boundary conditions**

Boundary value problems were solved using finite element computations to evaluate the stress-strain behavior of soft crystalline composites. Periodic boundary conditions were imposed in all directions to model the bulk behavior; we employed the method of fictitious nodes for implementing the generalized periodic boundary conditions as detailed in Sheng[17] and Danielsson.[18] The three-dimensional periodic boundary condition for a pair of material points (*A* and *B* at the periodic pair surfaces) can be applied as follows,

$$\mathbf{u}_A - \mathbf{u}_B = \left(\bar{\mathbf{F}} - \mathbf{I}\right) \cdot \left(\mathbf{X}_A - \mathbf{X}_B\right), \tag{1}$$

where $\mathbf{u}$ is the local displacement, $\bar{\mathbf{F}}$ is the prescribed macroscopic deformation gradient for a periodic unit cell, $\mathbf{X}$ is the coordinate vector for the undeformed reference body, and $\mathbf{I}$ is the 2nd order identity tensor. Equation (1) provides kinematic constraints for the material points subject to the periodic boundary conditions. The macroscopic stress-strain behavior of the soft composites was then computed using the principle of virtual work for the unit cell under the prescribed deformation condition such that an internal virtual work due to admissible variations is balanced with an external virtual work, as follows,

$$\delta W_{\text{int}} = \delta W_{\text{ext}}. \tag{2}$$

The internal virtual work can be expressed in terms of the Piola (engineering) stress and the deformation gradient (or displacement gradient), as follows,

$$\delta W_{\text{int}} = \int_{V_0} \mathbf{P}\left(\mathbf{X}\right) : \delta \mathbf{F}\left(\mathbf{X}\right) dV_0 = V_0 \bar{\mathbf{P}} : \delta \bar{\mathbf{F}} = V_0 \bar{\mathbf{P}} : \delta \bar{\mathbf{H}}, \tag{3}$$

where $\mathbf{P}$ is the local first Piola stress and V_0 is the volume at the reference configuration, $\mathbf{F} \equiv \dfrac{\partial \mathbf{x}}{\partial \mathbf{X}}$ is the local deformation gradient that maps the material points ($\mathbf{X}$) at the reference to the spatial points ($\mathbf{x}$) at the deformed configuration, $\bar{\mathbf{H}} \equiv \bar{\mathbf{F}} - \mathbf{I}$ is the macroscopic displacement gradient, and (:) denotes the inner product of tensors. The external virtual work may be written as,

$$\delta W_{\text{ext}} = \int_{S_0} \mathbf{P}\left(\mathbf{X}\right) \mathbf{n}_0 \cdot \delta \mathbf{u}\left(\mathbf{X}\right) dS_0 = \int_{S_0} \mathbf{t}_0\left(\mathbf{X}\right) \cdot \delta \mathbf{u}\left(\mathbf{X}\right) dS_0, \tag{4}$$

where $\mathbf{P}$ is the local Piola stress, $\mathbf{t}_0 \equiv \mathbf{P}\mathbf{n}_0$ is the surface traction, $\delta \mathbf{u}$ is the virtual displacement in the reference configuration, and $\mathbf{n}_0$ is the outward unit vector normal to the surface. For the periodic unit cell, the external virtual work may be computed, as follows,

$$\delta W_{\text{ext}} = \boldsymbol{\Xi} : \delta \boldsymbol{\xi}, \tag{5}$$

where ξ_{ij} are the generalized degrees of freedom or displacement components of the fictitious nodes (j = 1, 2, 3) and Ξ_{ij} are the work conjugate generalized forces for the generalized degrees of freedom, ξ_{ij}. Here, the admissible variation of the generalized coordinates is identical to the variation of macroscopic displacement gradient, i.e. $\delta\boldsymbol{\xi} = \delta\bar{\mathbf{H}}$. By using Equation (3), (4) and (5), the macroscopically "averaged" stress response in the periodic unit cell can be simply computed as follows,

$$\bar{\mathbf{P}} = \frac{1}{V_0}\int_{V_0} \mathbf{P}(\mathbf{X})\,dV_0 = \frac{1}{V_0}\boldsymbol{\Xi}. \qquad (6)$$

The fully three-dimensional periodic boundary conditions were implemented and applied for all of the numerical simulations of the composites in this work.

- **Single crystal elasticity**

A generalized three-dimensional anisotropic linear elasticity is expressed by stress ($\boldsymbol{\sigma}$)-strain ($\boldsymbol{\varepsilon}$) relationships of the form $\boldsymbol{\sigma} = \mathbf{C}\boldsymbol{\varepsilon}$ or $\boldsymbol{\varepsilon} = \mathbf{S}\boldsymbol{\sigma}$, where **C** and **S** are the fourth order stiffness and compliance tensors, respectively. The stiffness or compliance tensor has 21 independent components of elastic moduli in a fully anisotropic elastic material, which are commonly expressed as a symmetric 6 by 6 matrix using the Voigt notation. The independent elastic moduli are then reduced to three components in a cubic single crystal material through its major symmetries. The three independent elastic moduli of the fourth order elastic modulus tensor can be given by $\{C_{11}, C_{12}, C_{44}\}$ or $\{S_{11}, S_{12}, S_{44}\}$ in the Voigt notation. To compute the stiffness or compliance tensors, the periodic unit cells were subjected to simple deformation conditions including uniaxial compression, simple shear and uniform compaction. Once the three independent elastic moduli are found in a given cubic crystal, the directional Young's modulus in an arbitrary crystal orientation of $[l_x\, l_y\, l_z]$ can be computed by,

$$E[l_x\, l_y\, l_z] = \frac{1}{S_{11}[l_x\, l_y\, l_z]}, \qquad (7)$$

$$S_{11}[l_x\, l_y\, l_z] = S_{11} - 2\left(S_{11} - S_{12} - \frac{1}{2}S_{44}\right)\left(l_x^2 l_y^2 + l_y^2 l_z^2 + l_z^2 l_x^2\right), \qquad (8)$$

where $\{S_{11}, S_{12}, S_{44}\}$ is the compliance in the original crystallographic axes.

- **Constitutive behavior of base materials**

A Neo-Hookean hyperelastic representation was chosen to describe the constitutive behaviors of the pure hard and soft components used in the composites. The Cauchy (true) stress can be expressed by[19],

$$\mathbf{T} = \frac{\mu}{J}\left(\mathbf{F}^{*}\mathbf{F}^{*T}\right)' + K\left(J-1\right)\mathbf{I}, \tag{12}$$

where $\mathbf{F}^{*} = J^{-1/3}\mathbf{F}$ is the isochoric part of the deformation gradient, $\mu = \dfrac{E}{2\left(1+\nu\right)}$ is the elastic shear modulus, $K = \dfrac{E}{3\left(1-2\nu\right)}$ is the bulk modulus, ν is the Poisson's ratio, and $\left(\mathrm{g}\right)'$ denotes the deviatoric part of a given tensor, i.e. $\left(\mathrm{g}\right)' = \left(\mathrm{g}\right) - \frac{1}{3}tr\left(\mathrm{g}\right)\mathbf{I}$. The elastic moduli we used for the models were: E = 0.56, 1.92, 2.87, 5.27, 8.22, and 56.0 MPa, ν = 0.49, 0.48, 0.47, 0.46, 0.45 and 0.45 for s, h1, h2, h3, h4 and h5, respectively. Additionally, to reduce the inelastic effect in the materials, the rate of straining was chosen to be very low (under 0.001 /s), which was also used in the compression tests of the composites. **Figure 12** shows the stress-strain behaviors of the hard and soft materials under compression in experiments and models. The predicted stress-strain curves nicely matched those in experiments.

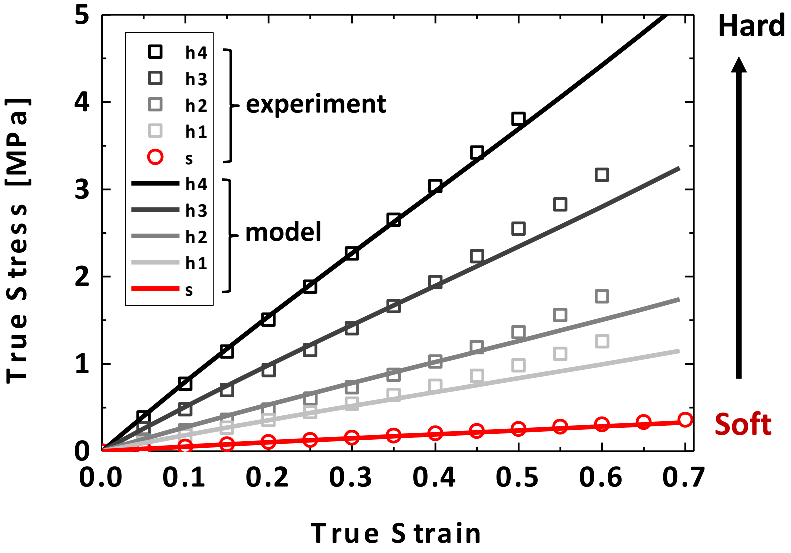

Figure 12 Representative stress-strain behavior of the hard ("h1" ~ "h4") and soft material ("s") used in the composites under compression (symbols: experiment; lines: model)

Acknowledgements

Authors gratefully acknowledge financial support from BASF. Authors also acknowledge fruitful discussions on the morphological micromechanics with Professor David M. Parks at MIT. Use of the 3D printing facilities at the Wyss Institute at Harvard University to fabricate the prototypes is gratefully acknowledged.

REFERENCE

[1] A. J. Crosby, J. Y. Lee, Polymer reviews 2007, 47, 217; M. E. Launey, R. O. Ritchie, Advanced Materials 2009, 21, 2103.

[2] D. W. Van Krevelen, K. Te Nijenhuis, *Properties of polymers: their correlation with chemical structure; their numerical estimation and prediction from additive group contributions*, Elsevier, 2009; S. R. White, N. R. Sottos, P. H. Geubelle, J. S. Moore, M. R. Kessler, S. R. Sriram, E. N. Brown, S. Viswanathan, Nature 2001, 409, 794.

[3] S. Carter, J. Scott, P. Brock, Applied Physics Letters 1997, 71, 1145; S. H. Foulger, P. Jiang, A. Lattam, D. W. Smith, J. Ballato, D. E. Dausch, S. Grego, B. R. Stoner, Advanced Materials 2003, 15, 685.

[4] P. M. Ajayan, L. S. Schadler, P. V. Braun, *Nanocomposite science and technology*, John Wiley & Sons, 2006; R. F. Landel, L. E. Nielsen, *Mechanical properties of polymers and composites*, CRC Press, 1993; Y.-W. Mai, Z.-Z. Yu, *Polymer nanocomposites*, Woodhead publishing, 2006.

[5] J. H. Lee, J. P. Singer, E. L. Thomas, Advanced Materials 2012, 24, 4782; S. Torquato, International Journal of Solids and Structures 2000, 37, 411; S. Torquato, *Random heterogeneous materials: microstructure and macroscopic properties*, Vol. 16, Springer Science & Business Media, 2013.

[6] F. S. Bates, G. H. Fredrickson, Annual Review of Physical Chemistry 1990, 41, 525; F. S. Bates, G. H. Fredrickson, Physics today 2008, 52, 32; P. C. Hiemenz, T. P. Lodge, *Polymer chemistry*, CRC press, 2007; I. W. Hamley, *The physics of block copolymers*, Vol. 19, Oxford University Press New York, 1998.

[7] H. Cho, R. G. Rinaldi, M. C. Boyce, Soft Matter 2013, 9, 6319; J. H. Lee, C. Y. Koh, J. P. Singer, S. J. Jeon, M. Maldovan, O. Stein, E. L. Thomas, Advanced Materials 2014, 26, 532; L. Wang, J. Lau, E. L. Thomas, M. C. Boyce, Advanced Materials 2011, 23, 1524; J. Yi, M. Boyce, G. Lee, E. Balizer, Polymer 2006, 47, 319.

[8] J.-H. Lee, L. Wang, M. C. Boyce, E. L. Thomas, Nano letters 2012, 12, 4392; L. Wang, M. C. Boyce, C. Y. Wen, E. L. Thomas, Advanced Functional Materials 2009, 19, 1343; W. Ma, C. Yang, X. Gong, K. Lee, A. J. Heeger, Advanced Functional Materials 2005, 15, 1617.

[9] K. Bertoldi, M. Boyce, Physical Review B 2008, 77, 052105; M. R. Bockstaller, R. A. Mickiewicz, E. L. Thomas, Advanced Materials 2005, 17, 1331; J. Ge, Y. Yin, Angewandte Chemie International Edition 2011, 50, 1492.

[10] K. Bertoldi, M. Boyce, S. Deschanel, S. Prange, T. Mullin, Journal of the Mechanics and Physics of Solids 2008, 56, 2642; B. Florijn, C. Coulais, M. van Hecke, Physical review letters 2014, 113, 175503; T. Mullin, S. Deschanel, K. Bertoldi, M. Boyce, Physical review letters 2007, 99, 084301; S. Shan, S. H. Kang, J. R. Raney, P. Wang, L. Fang, F. Candido, J. A. Lewis, K. Bertoldi, Advanced Materials 2015, 27, 4296.

[11] B. Mosadegh, P. Polygerinos, C. Keplinger, S. Wennstedt, R. F. Shepherd, U. Gupta, J. Shim, K. Bertoldi, C. J. Walsh, G. M. Whitesides, Advanced Functional Materials 2014, 24, 2163; D. Yang, B. Mosadegh, A. Ainla, B. Lee, F. Khashai, Z. Suo, K. Bertoldi, G. M. Whitesides, Advanced Materials 2015, 27, 6323.

[12] S. Rudykh, M. C. Boyce, Physical review letters 2014, 112, 034301; S. Shan, S. H. Kang, P. Wang, C. Qu, S. Shian, E. R. Chen, K. Bertoldi, Advanced Functional Materials 2014, 24, 4935.

[13] A. Tuteja, W. Choi, J. M. Mabry, G. H. McKinley, R. E. Cohen, Proceedings of the National Academy of Sciences 2008, 105, 18200; W. Choi, A. Tuteja, S. Chhatre, J. M. Mabry, R. E. Cohen, G. H. McKinley, Advanced Materials 2009, 21, 2190.

[14] D. Terwagne, M. Brojan, P. M. Reis, Advanced Materials 2014; Z. Yan, F. Zhang, J. Wang, F. Liu, X. Guo, K. Nan, Q. Lin, M. Gao, D. Xiao, Y. Shi, Advanced Functional Materials 2016.

[15] Stratasys, 2014.

[16] J. F. Nye, *Physical properties of crystals: their representation by tensors and matrices*, Oxford university press, 1985.

[17] N. Sheng, Massachusetts Institute of Technology, Cambridge 2006.

[18] M. Danielsson, Massachusetts Institute of Technology, Cambridge 2003.

[19] R. W. Ogden, *Non-linear elastic deformations*, Courier Dover Publications, 1997.